

Supplement to: Reducing intrinsic loss in superconducting resonators by surface treatment and deep etching of silicon substrates

A. Bruno,¹ G. de Lange,¹ S. Asaad,¹ K. L. van der Enden,¹ N. K. Langford,¹ and L. DiCarlo¹

¹*QuTech Advanced Research Center and Kavli Institute of Nanoscience,
Delft University of Technology, Lorentzweg 1, 2628 CJ Delft, The Netherlands*

(Dated: June 5, 2015)

This supplement provides experimental details and data sets supporting claims made in the main text. First, we present design and fabrication details for three device generations that we have measured: Device C (reported in the main text) and devices from Sets A and B (reported below). We then describe several technical details of the measurement system: the measurement setup and device shielding, the fitting of the complex-valued transmission spectra, and the procedure for estimating $\langle n_{\text{ph}} \rangle$. Next, we present measurement results for devices from Sets A and B. Finally, we discuss the results of XPS analysis of the pre-deposition substrate surface following different treatments.

DEVICES

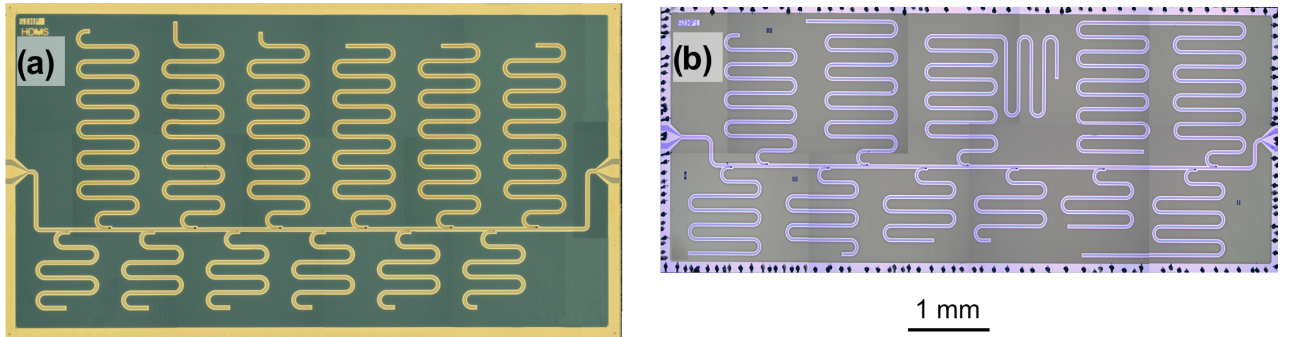


FIG. S1: (a) Optical image of HMDS-treated device from Set B (Set B used the same layout as Set A). The feedline and the lower 6 resonators are etched by RIE while the top 6 resonators are patterned by DRIE. Frequencies for the RIE and DRIE resonators are centered around 7 and 4 GHz, respectively. (b) Optical image of Device C (HMDS+DRIE). The feedline is patterned using RIE, but all resonators are fabricated using DRIE with frequencies spanning 2 to 11 GHz.

We begin our investigation of dielectric losses in CPW resonators starting from the existing best practice of fluorine-based etching [1] of NbTiN superconducting thin films [2] on silicon substrates prepared with an HF dip to remove lossy oxide layers [3].

Devices in Sets A and B had identical layouts (Fig. S1a). Each device contained 6 RIE resonators with frequencies ~ 7 GHz (spaced by ~ 100 MHz; see results in Figs. S4 and S6) and 6 DRIE resonators with frequencies ~ 4 GHz (also spaced by ~ 100 MHz; see results in Figs. S5 and S7). Note that DRIE is used to etch through both the NbTiN and silicon substrate using a single etching step with a single mask, so there is no possibility for misalignment between the etched NbTiN and the silicon trenches. As discussed in the main text, the misalignment between DRIE and RIE structures is less than 100 nm, limited only by the e-beam lithography. In each set, we fabricated one device using the standard HF-only substrate treatment (green dashed curves in Figs. S4–S7) and one device using the HF+HMDS substrate treatment (solid red curves in Figs. S4–S7). In Sets A and B, the DRIE recipe is slightly different from the recipe described in the main text (for Device C). For these sets, the plasma power used in the DRIE etching step was set at 1800 W. At the end of the deep etch process, the samples underwent an additional etch with an SF₆ inductively coupled plasma (20 mTorr, 1800 W, 60 s with no alternating passivation step). This removed the fluorocarbon passivation and created a slightly isotropic etch profile. The fabrication was otherwise almost identical for Sets A and B, with the NbTiN film ~ 160 nm thick and the DRIE etch ~ 80 μm deep. The only difference was that the devices in Set B were fabricated with the inclusion of a short (20 sec) additional fluorocarbon side-wall passivation step in the DRIE recipe after the isotropic etch, while no such final step was included in the devices from Set A.

Device C (recipe and data in main text) only included DRIE resonators fabricated using the combined HF+HMDS surface treatment. We used a thicker (~ 300 nm) NbTiN film, and kept the DRIE etch depth the same (~ 80 μm). The device had 10 resonators with frequencies between 2 and 11 GHz. The plasma power in the etching step in the DRIE recipe was increased to 2200 W to reduce the feature size of the side-wall scalloping.

MEASUREMENT SETUP

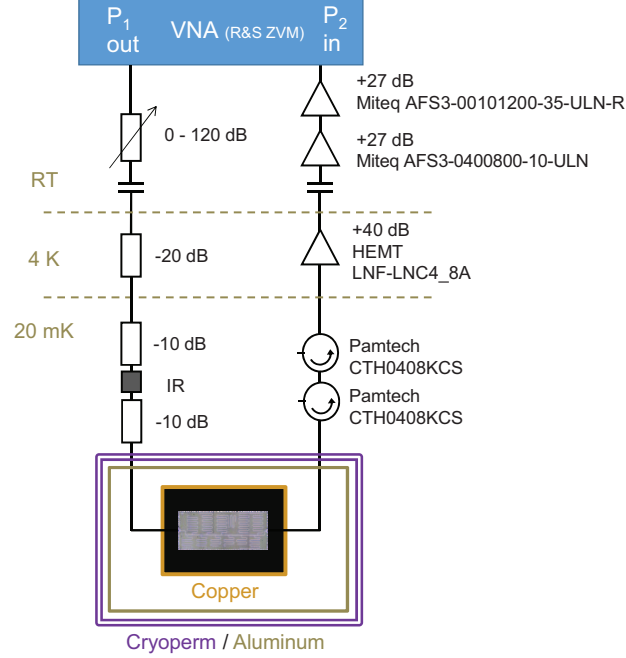


FIG. S2: Measurement setup used for resonator characterization in the $^3\text{He}/^4\text{He}$ dilution refrigerator (Leiden Cryogenics CS81): microwave schematic, magnetic shields (two Cryophy, one aluminum), IR filters (home-made Eccosorb filters), and IR adsorbers (inner surface of the inner Cu radiation shield, coated with Stycast 2850 and silicon carbide powder).

In an effort to minimize resonator losses induced by non-equilibrium quasiparticles [4] and magnetic vortex displacement [5], we mount the samples inside several layers of shielding (Fig. S2). Specifically, we anchor the PCB-mounted sample directly to a copper cold finger connected to the mixing chamber of the dilution refrigerator. The sample is then enclosed in a copper can, the inner surface of which is coated in a mixture of Stycast 2850 and silicon carbide granules with diameters between 15 and 1000 μm . This can is enclosed in a second can made from aluminum. This is finally enclosed in two layers of cryogenic magnetic shielding (1-mm-thick Cryophy, Magnetic Shields Ltd). Coaxial cables enter the sample chamber through tubulations in the lid of the outer layer of magnetic shielding to reduce the impact of open holes on the shielding effectiveness. Extra radiation shielding is provided by home-made in-line Eccosorb filters in the input coaxial line mounted outside the magnetic shields at the mixing chamber stage.

Data fitting

The transmission through the full measurement chain near one resonance is shown in Fig. S3. We fit the S_{21} curves following the method presented in Ref. 6. Equation 11 in Ref. 6 describes the general form of a microwave resonator transmission measurement with a number of non-ideal elements, including both inductive and capacitive coupling, and impedance mismatch in the feedline:

$$S_{21} = A \left(1 - \frac{\frac{Q_i}{|Q_e|} e^{i\theta}}{1 + 2iQ_i \frac{f - f_r}{f_r}} \right). \quad (\text{S1})$$

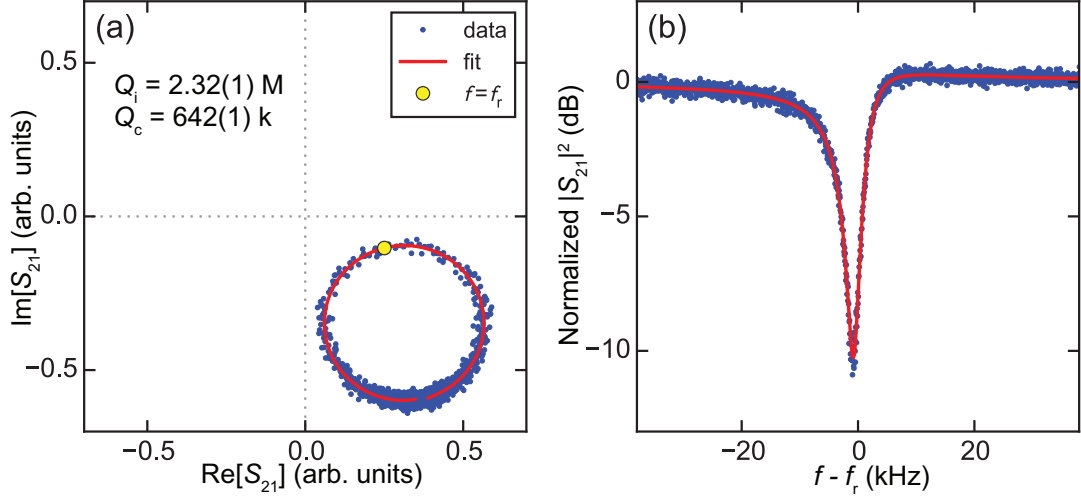


FIG. S3: Typical measured response of a CPW resonator around its resonance frequency, and fit. Data taken from DRIE resonator with $f_r = 3.68$ GHz at $\langle n_{\text{ph}} \rangle \sim 10$ photons (Fig. 3 of main text). Panel (a) shows the trajectory of S_{21} in the complex plane with a fit (red line) of Eq. S2. (b) Normalized $|S_{21}|^2$ calculated from the data and fit in (a).

Here, f_r is the resonance frequency, A is the transmission amplitude away from resonance, Q_1 is the loaded quality factor of the resonator, related to Q_i and Q_c by $1/Q_1 = 1/Q_c + 1/Q_i$, and $Q_e = |Q_e| \exp(-i\theta)$ is a complex-valued quality factor related to Q_c via $1/Q_c = \text{Re}(1/Q_e)$. The imaginary part of $1/Q_e$ gives rise to an asymmetry in the resonator lineshape. We further modify Eq. S1 as follows:

$$S_{21} = A \left(1 + \alpha \frac{f - f_r}{f_r} \right) \left(1 - \frac{\frac{Q_1}{|Q_e|} e^{i\theta}}{1 + 2iQ_1 \frac{f - f_r}{f_r}} \right) e^{i(\phi_v f + \phi_0)}. \quad (\text{S2})$$

Here, α allows a linear variation in the overall transmission chain in the narrow frequency range around any given resonance, and ϕ_v and ϕ_0 account for the propagation delay to and from the sample. An example best fit of Eq. S2 to data is also shown in Fig. S3.

Calibration of the average number of photons in the resonator

To estimate $\langle n_{\text{ph}} \rangle$, we calibrated the signal input line and the home-made eccosorb filter at low temperature in order to estimate the power P_{in} at the feedline input. To calculate $\langle n_{\text{ph}} \rangle$ from P_{in} , we note that the reflected and transmitted powers (ignoring feedline mismatch) are respectively given by:

$$P_{\text{refl}} = P_{\text{in}} |S_{11}|^2, \\ P_{\text{trans}} = P_{\text{in}} |S_{21}|^2,$$

where $S_{21} = Q_c / (Q_c + Q_i)$ and $S_{11} = S_{21} - 1 = -Q_i / (Q_c + Q_i)$ are the usual scattering parameters for a resonator-shunted feedline probed near resonance [7]. The power absorbed in the resonator is therefore:

$$P_{\text{abs}} = P_{\text{in}} - P_{\text{refl}} - P_{\text{trans}} = \frac{2Q_1^2}{Q_c Q_i} P_{\text{in}}.$$

P_{abs} can also be written using the definition of internal loss rate κ_i :

$$P_{\text{abs}} = \langle n_{\text{ph}} \rangle \hbar \omega_r \kappa_i, \\ = \langle n_{\text{ph}} \rangle \frac{\hbar \omega_r^2}{Q_i}.$$

Combining these equations then gives the relation between $\langle n_{\text{ph}} \rangle$ and P_{in} :

$$\langle n_{\text{ph}} \rangle = \frac{2}{\hbar \omega_{\text{r}}^2} \frac{Q_{\text{l}}^2}{Q_{\text{c}}} P_{\text{in}}.$$

Due to the difficulty in accounting for all reflections in the full measurement line, these values can be interpreted as an estimated upper limit to $\langle n_{\text{ph}} \rangle$.

RESULTS FROM SETS A AND B AT 20 mK

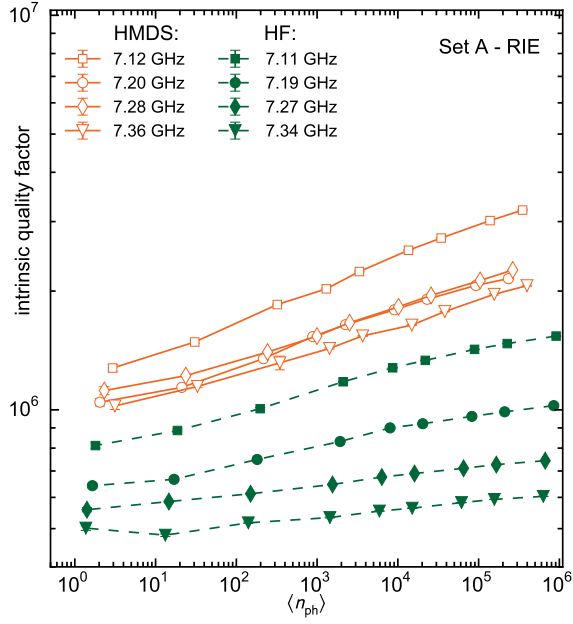


FIG. S4: Comparison between HF and HMDS surface treatment of RIE resonators from Set A.

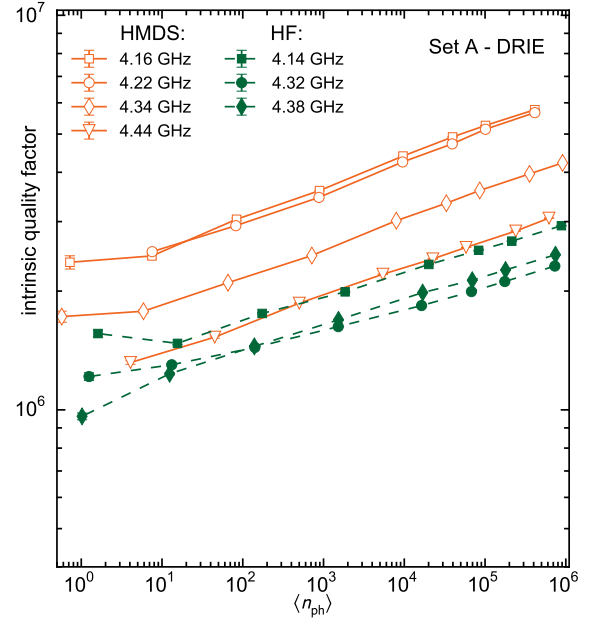


FIG. S5: Comparison between HF and HMDS surface treatment of DRIE resonators from Set A.

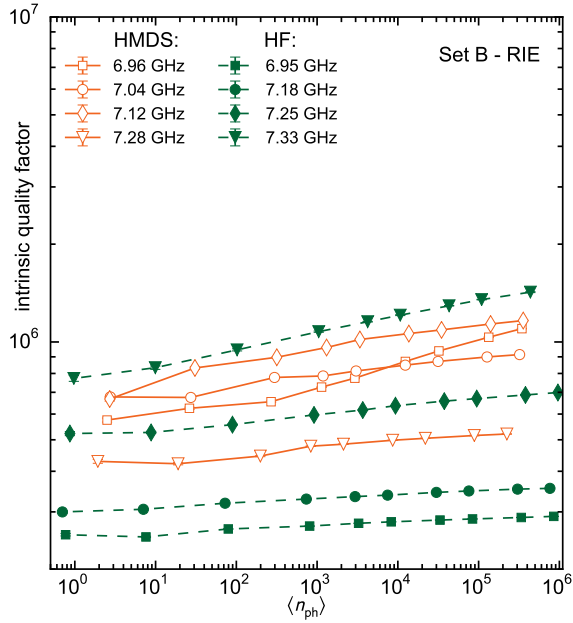


FIG. S6: Comparison between HF and HMDS surface treatment of RIE resonators from Set B.

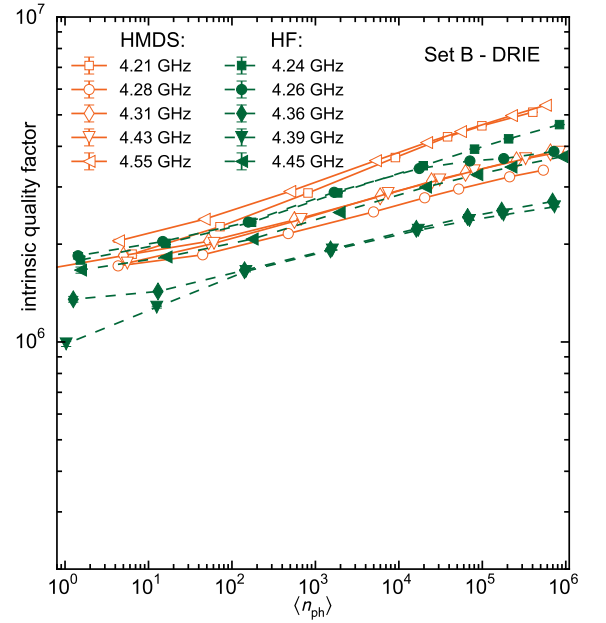


FIG. S7: Comparison between HF and HMDS surface treatment of DRIE resonators from Set B.

XPS DATA

We performed XPS surface analysis of Si substrates in order to estimate surface oxygen uptake during the HMDS treatment following the HF dip, as well as during the approximately two-minute interval between finishing the surface preparation and loading the sample into the high-vacuum chamber ($P_{\text{base}} = 2 \times 10^{-8}$ Torr) for NbTiN deposition.

Figure S8a shows that the standard HF surface treatment already removes all signatures of SiO from the substrate surface. No discernible change is observed when substrates are placed in a mixed nitrogen-HMDS atmosphere, created by HMDS bubbling, following the HF dip. Figure S8b shows the XPS spectrum after subsequent exposures to air. While measurement directly after fast loading does not reveal a Si-O peak, subsequent exposures of the sample to atmospheric conditions show the onset of one, indicating oxygen adsorption by the substrate surface. We also made the same measurements for a silicon substrate which was prepared only with an HF dip, but no HMDS bubbling. The results (data not shown) were indistinguishable from those in Fig. S8b, indicating that HMDS does not alter reoxidation dynamics of the Si substrate.

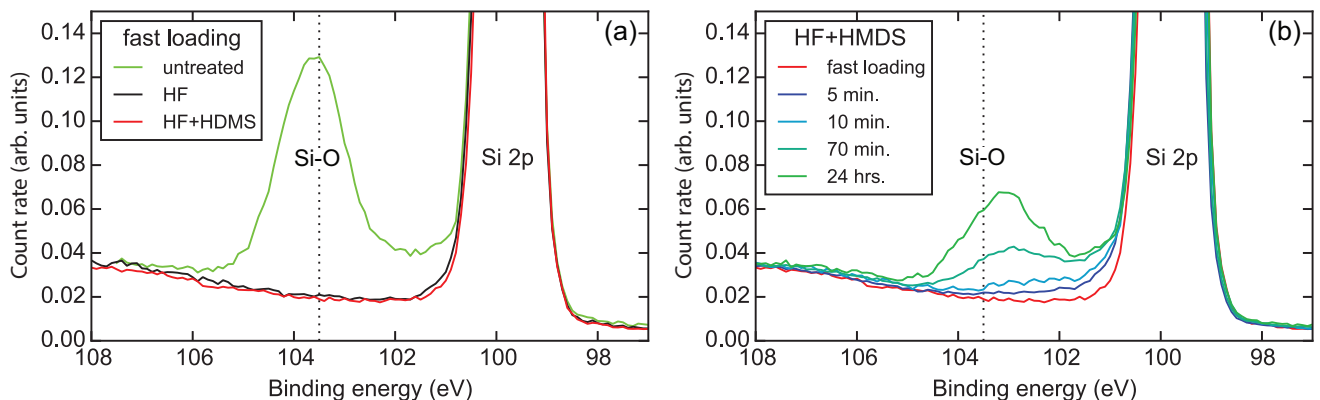


FIG. S8: XPS analysis after fast loading of substrates (~ 2 min after surface processing). (a) XPS spectrum of the Si-O peak at 103.5 ± 0.3 eV for: an untreated Si surface with native oxides (green), a Si surface treated by HF dip only (black), and a Si surface treated by HF dip and HMDS bubbling (red) as described in the main text. (b) Time evolution of the XPS Si-O peak for a Si surface treated by HF dip and HMDS bubbling after subsequent exposures to atmospheric conditions (times indicated in the legend). (We thank V. de Rooij and E. van Veldhoven for carrying out the XPS measurements.)

-
- [1] M. Sandberg, M. R. Vissers, J. S. Kline, M. Weides, J. Gao, D. S. Wisbey, and D. P. Pappas, *Appl. Phys. Lett.* **100**, 262605 (2012).
 - [2] R. Barends, N. Vercruyssen, A. Endo, P. De Visser, T. Zijlstra, T. Klapwijk, and J. Baselmans, *Appl. Phys. Lett.* **97**, 033507 (2010).
 - [3] D. S. Wisbey, J. Gao, M. R. Vissers, F. C. da Silva, J. S. Kline, L. Vale, and D. P. Pappas, *J. Appl. Phys.* **108**, 093918 (2010).
 - [4] R. Barends, J. Wenner, M. Lenander, Y. Chen, R. C. Bialczak, J. Kelly, E. Lucero, P. O'Malley, M. Mariani, D. Sank *et al.*, *Appl. Phys. Lett.* **99**, 113507 (2011).
 - [5] D. Bothner, T. Gaber, M. Kemmler, D. Koelle, and R. Kleiner, *Appl. Phys. Lett.* **98**, 102504 (2011).
 - [6] M. S. Khalil, M. J. A. Stoutimore, F. C. Wellstood, and K. D. Osborn, *J. Appl. Phys.* **111**, 054510 (2012).
 - [7] R. Barends, Ph.D. thesis, Delft University of Technology (2009).